Aerodynamic Control for a Subsonic Diffuser

Thesis by
Wei-Jen Su

In partial fulfillment of the requirements
for the degree of
Engineer

Graduate Aeronautical Laboratories
California Institute of Technology
Pasadena, California 91125

2001
(Submitted April 17, 2001)

Acknowledgement

First and most importantly, I wish to thank my advisor, Prof. Paul Dimotakis, to whom I am indebted for his advice, and who made this thesis a reality.

I wish to thank Earl Dahl for his technical assistance and expertise. Without him, it would have probably taken a couple of more years to complete the experimental tests. Also, I wish to thank Dr. Dan Lang for his help with the electronics and computer system problems that I encountered.

I feel very lucky and grateful to work with my collaborator Michael Johnson. His help was invaluable. Also, I wish to thank Dr. Michael Slessor for his tutoring of the experimental facility and the design of the new diffuser. I also need to be thankful for advice from Jimmy Fung, Jerry Shan, and Dr. Chris Bond.

Finally, I wish to thank my dad, Dr. Yu-Chang Su, who provided me the encouragement necessary to finish this thesis.

The Air Force Office of Scientific Research funded this work under Grant numbers F49620-98-1-0052 and F49620-01-1-0006.

Abstract

Experiments have been conducted in the GALCIT Supersonic Shear Layer Facility to investigate some aspects of mass injection in subsonic diffusers.

The goal of the experiment is to study aerodynamic control in subsonic diffusers by investigating downstream velocity profiles. These experiments were designed to address several key issues like effects due to velocity change (for one-stream and two-stream flows), and effects due to density variation. The effect of the separation bubble (stall flow) on the performance of the diffuser has also been investigated.

One-stream experiments were performed with non-reacting (cold) runs using N_2 in the high-speed section at different velocities and zero velocity at the low-speed section. Detailed analysis of data obtained shows a slight dependency of the reattachment point of the separation bubble on Reynolds number. As the flow rate in the high-speed section increases, the reattachment point of the separation bubble shifted slightly downstream. Two-stream flow (low- and high-speed sections) experiments were performed using N_2 in the high-speed section and a density-matched mixture of Argon/Helium in the low-speed section. As the mass injection is increased in the low-speed section, the reattachment point of the separation bubble moved further downstream. While keeping the same velocity ratio (low- and high-speed sections), as the overall flow velocity increases, the reattachment point moved further downstream. Also, experiments with a higher density ratio using Argon in the low-speed section and N_2 in the high-speed section were performed. As the density of the low-speed section increases, the reattachment point of the separation bubble moved upstream due to shear-layer entrainment effect. Finally, as the reattachment point of the separation bubble shifted further downstream, the diffuser pressure coefficient decreases, therefore, the performance of the diffuser is degraded.

Schlieren flow visualization and pressure probes were used in the experiments.

Contents

CHAPTER 1

Introduction and background

A diffuser is an expansion or area-increasing device used to reduce the velocity of the fluid and recover pressure. Early Roman (about 100 A.D.) water supply system customers invented the diffuser since the piping system was billed according to pipe size (Rouse and Ince 1957). The ingenious customers discovered that they could increase the flow rate keeping the same pipe size by flaring the outlet section of the pipe.

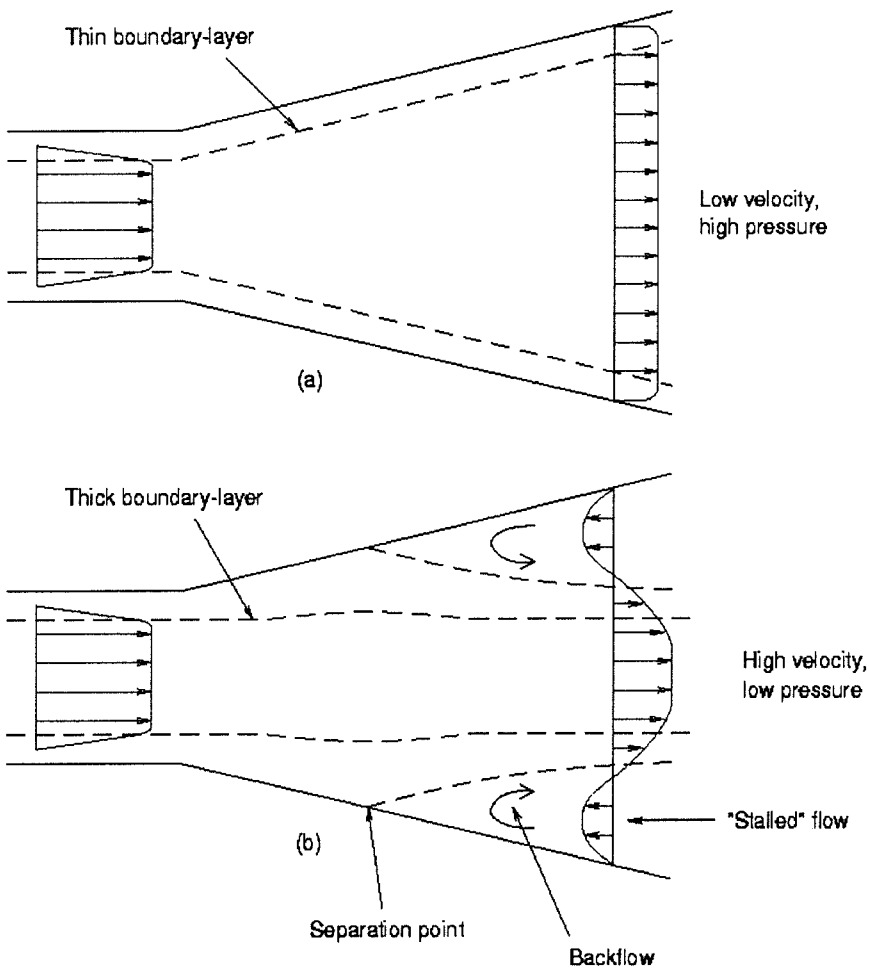

Fig. 1.1: Diffuser performance: a) ideal performance, flow remains attached; b) poor performance, boundary-layer separation (White 1999).

Before 1950, diffuser design was a combination of art, luck, and empiricism. Small changes in diffuser design parameters caused large changes in performance. After 1950, engineers mastered the way to design diffusers to recover pressure and reduce kinetic energy of the ducted flow. This was achieved with improvements in flow visualization system and measurement instruments (White 1999).

A subsonic diffuser works as follows. In a straight pipe, the exhaust static pressure is the same as atmospheric pressure. Therefore, there is a pressure recovery associated with that. But, if you increase the exhaust area, the static pressure at exhaust is again atmospheric pressure and using Bernoulli's equation, the pressure at the upstream of the diffuser will be lower. Therefore, the diffuser pipe will have a better pressure recovery than without the diffuser. This is only true if you do not have a stalled flow or separation bubble generated within the diffuser (recirculation zone downstream of a ramp), as seen in Fig. 1.1a and Fig. 1.1b. Flow separation prevents full pressure recovery, increasing pressure at the inlet and the power required to sustain internal flow. Flow separation occurs when the pressure gradient is adverse (if pressure increases in the direction of the flow, $\partial p/\partial x > 0$) and the point of separation is at $\partial u/\partial y = 0$ (see Fig. 1.2).

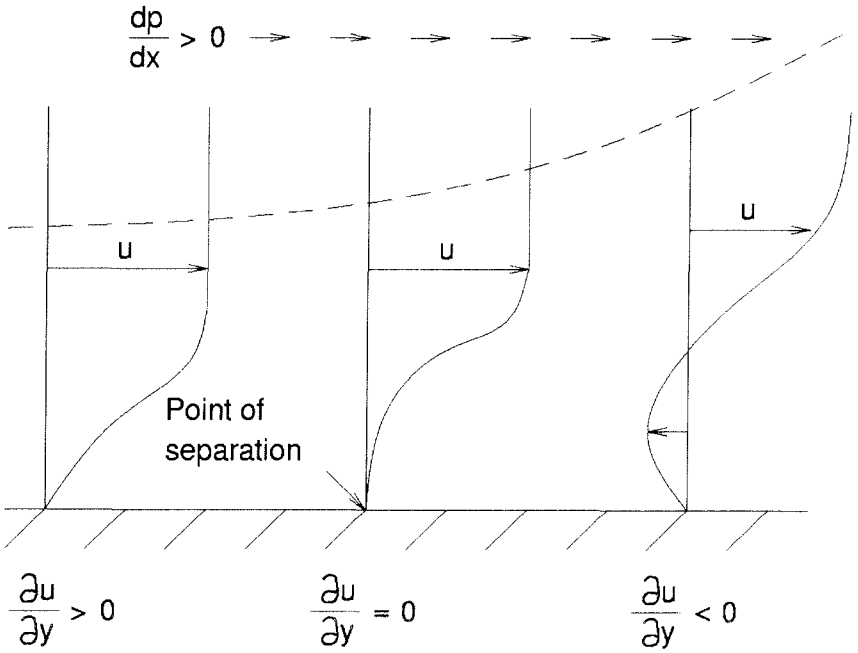

Fig. 1.2: Boundary-layer flow with adverse pressure gradient.

Fox and Kline (1962) mapped the region where stalled flow occurs depending on the angle and the length ratio of the diffuser. As seen in Fig. 1.3 (the abbreviation used in this figure is denoted in Fig. 1.4), the map shows basically four regions: no-stall region in which there is no flow separation, transitory-stall region for one separation bubble only, bistable steady stall for two separation bubbles, and finally jet flow. Current work falls in the region of transitory stall as shown in Fig. 1.3. Although the current work is for a single-sided diffuser (one side is a straight wall, the other has an angle), and not double-sided for the map shown in Fig. 1.4, the experimental results confirm that it has only one transitory stall.

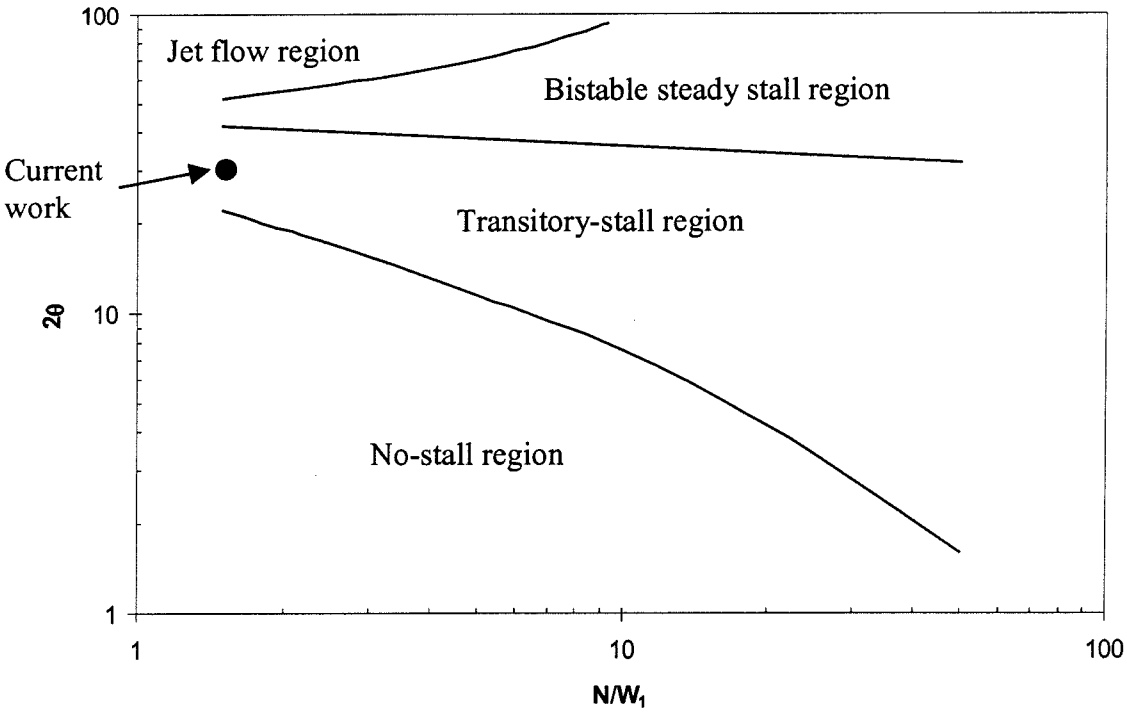

Fig. 1.3: Diffuser geometry and typical flow regimes (Fox and Kline 1962).

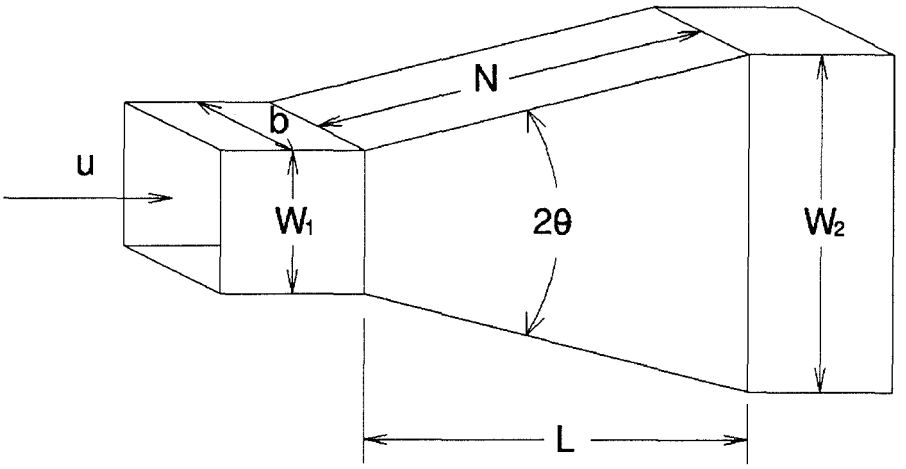

Fig. 1.4: Schematic of typical diffuser (Fox and Kline 1962).

The purpose of the current work is to investigate subsonic aerodynamic means of controlling the separation bubble (transitory stall bubble) through mass injection mainly by analyzing the downstream velocity profile. Variable-geometry configurations have the advantage that there are no moving parts, therefore, reducing the penalties in weight and complexity in internal flow control if a mechanical device is used (see Fig. 1.5). Also, the work investigates the effect of the separation bubble on the performance of the diffuser.

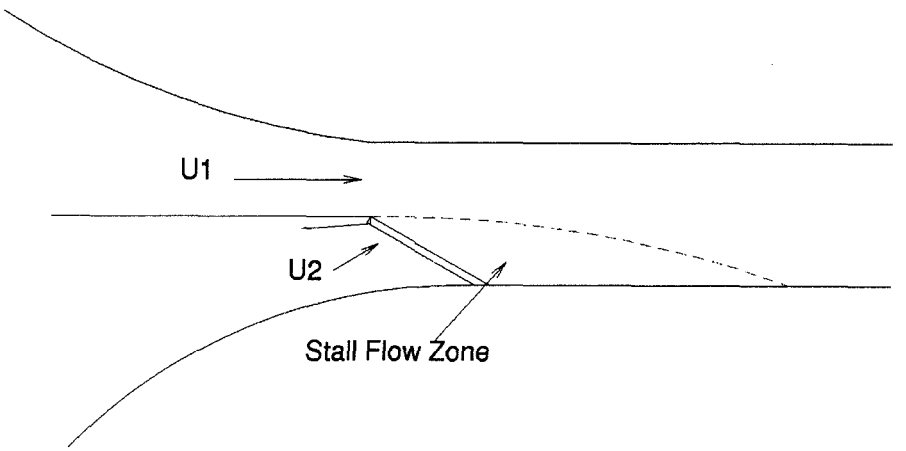

Fig. 1.5: Current diffuser.

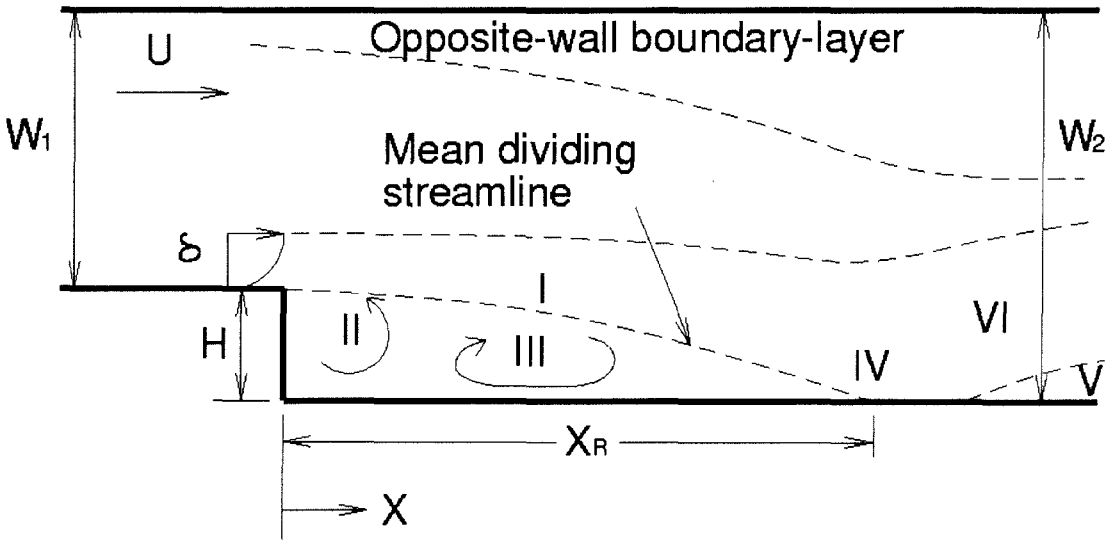

Flow zones:

I separated shear layer
II corner eddy
III backflow zone
IV reattachment zone
V redeveloping near-wall flow
VI relaxing outer shear layer

Fig. 1.6: Geometry and flow zones for reattachment in the single-sided planar sudden expansion (Westphal, Johnston, and Eaton 1984).

Westphal, Johnston, and Eaton (1984) studied the flow zones from a single-sided planar sudden expansion, as shown in Fig. 1.6. Current work shows similar regions except the diffuser is at a 30 degree angle, therefore, there is no corner eddy region (shown as Region II in Fig. 1.6).

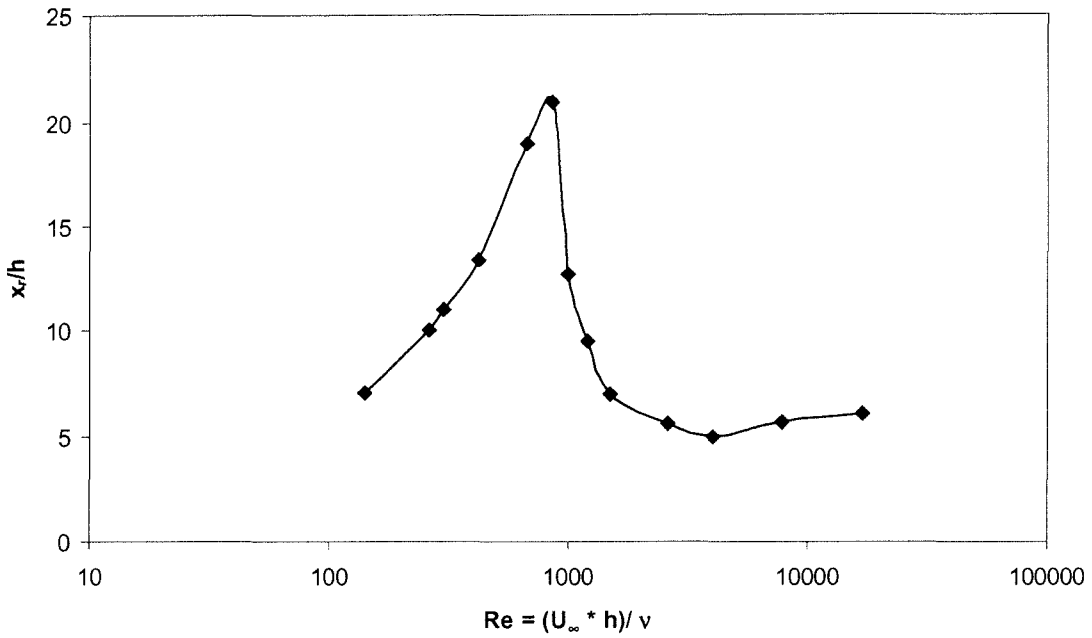

Fig. 1.7: Dependence of reattachment distance on Reynolds number for backstep (Sinha, Gupta, and Oberai 1981).

An issue to be studied is the reattachment point of the separation bubble. Research done by Sinha, Gupta, and Oberai (1981) (see Fig. 1.7) was similar to current work. Although the work done by Sinha, Gupta, and Overai (1981) falls in a lower Reynolds number range and is based on a backstep diffuser compared to current work. Their result, shown in Fig. 1.7, was extrapolated (assuming the reattachment point is constant as the Reynolds number increases after 10,000) and the result is shown in Fig. 1.8 for the current work. Song, DeGraaff, and Eaton (2000) reached the same conclusion, *i.e.*, that the reattachment point of a separation bubble (stall transition bubble) remains the same as Reynolds number changes. Current work showed that as the Reynolds number increased, the separation bubble increased slightly in size.

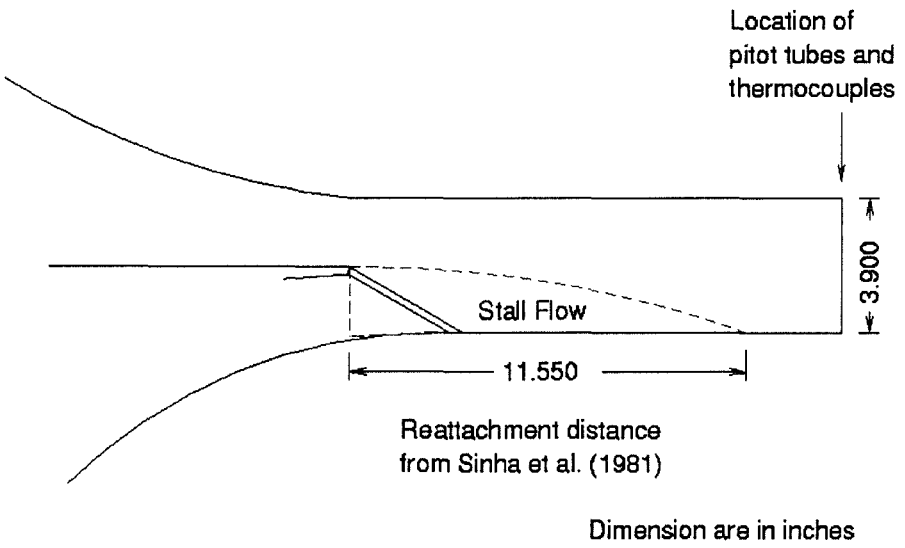

Fig. 1.8: Reattachment distance for current work based on Sinha, Gupta, and Oberai 1981.

Shear-layer growth is an important factor in the current work. Shear layer exhibit a dependence on incompressible-flow ($M = 0$, subscript $()_0$ denotes incompressible flow) growth rate, $\delta_0(x)/x$, on freestream-velocity and –density ratios, *i.e.*,

$$\frac{\delta_0}{x} \cong \frac{\delta_0}{x}\left(r \equiv \frac{U_2}{U_1}, s \equiv \frac{\rho_2}{\rho_1}\right) \tag{1.1}$$

In particular, geometric and similarity considerations employed by Dimotakis (1986) yield an estimate for a spatially growing layer given by,

$$\frac{\delta_0}{x}(r,s) \cong C_\delta \frac{(1-r)(1+s^{1/2})}{2(1+s^{1/2}r)}\left\{1-\frac{(1-s^{1/2})/(1+s^{1/2})}{1+2.9(1+r)/(1/r)}\right\}, \tag{1.2}$$

where C_δ is a constant independent of r and s. Experimental data are in accord with the overall dependence suggested by Eq. 1.2, however there is substantial variance in inferred values for C_δ, *i.e.*,

$$0.25 \leq C_{\delta} \leq 0.45, \tag{1.3}$$

especially between experiments performed in different facilities (Dimotakis 1991).

The results of this work are applicable all the way from internal combustion chambers to aerodynamic control for aircraft. For example, in jet engines, the air leaving the axial flow compressor passes through a diffuser before entering the combustion chamber. This flow may be distorted by wall boundary-layers, unsteady flow, and the mean velocity is not parallel to the centerline of the diffuser. This will affect the efficiency of the combustor and the overall pressure rise of the system.

CHAPTER 2

Facility, instrumentation, and measurements

2.1 Facility overview

The GALCIT Supersonic Shear Layer (S^3L) Facility is a two-stream, blow-down, wind tunnel, capable of attaining freestream Mach numbers all the way from incompressible to compressible gas-phase flow (high-speed section $M_1 \leq 3.2$ and low-speed section $M_2 \leq 1.13$). The current work was limited to $U_1 \leq 250$ m/s and $U_2 \leq 30$ m/s, in non-reacting and chemically reacting configurations. Additional details can be found in Hall and Dimotakis (1989), Hall (1991), Bond (1998), and Slessor (1998).

Fig. 2.1 shows the schematic of the facility. It operates with a run time of $t_{run} > t_{dat} \approx 2 - 6$ s, where t_{dat} is the data-recording time. Gas for the two freestreams is supplied by independent flow systems charged by standard bottle-gas supplies prior to the experimental run. By mixing different types of gases, one can vary the density ratio, specific heat ratio, etc.

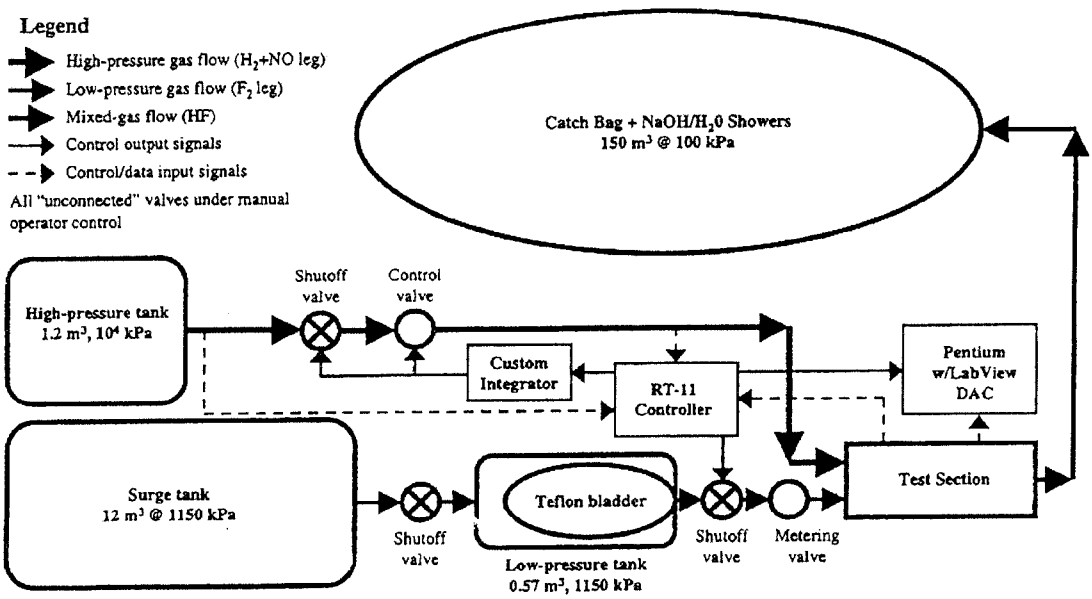

Fig. 2.1: Overall facility gas-flow schematic (Slessor 1998, Fig. 2.1).

The test section operates at static atmospheric pressure, or slightly less. This is the main difference from most other supersonic-flow facilities, whose test sections operate at much lower-pressure conditions to ease demands on upstream flow-supply systems.

The high-speed section freestream speed is maintained by plenum-pressure control, operated in either an open-loop (program-control) configuration, at low mass-flux conditions, or a closed-loop (nonlinear-feedback-control) configuration at moderate-to-high mass-flux conditions (Slessor 1998 has a more detailed explanation of the system). Gas is supplied to this plenum from a 1.2 m^3 pressure vessel, at a maximum pressure of 10^4 kPa. During blowdown, vessel pressure can drop by as much as 50%, which requires an active-control system. The gas in the vessel is maintained at a nearly constant temperature by rolled aluminum screen (large heat capacity) that occupies a fraction of the pressure-vessel volume.

The mass flux through the low-speed section (low-pressure plenum) is set by a choked metering valve kept fixed during each run. A calibration of the metering valve was performed and will be explained below. Gas to this plenum is supplied from a 0.57 m^3 vessel that encloses a bladder bag. This vessel is pressurized, in turn, by a N_2-filled, large-volume surge tank whose pressure falls by 3 – 5% during a run.

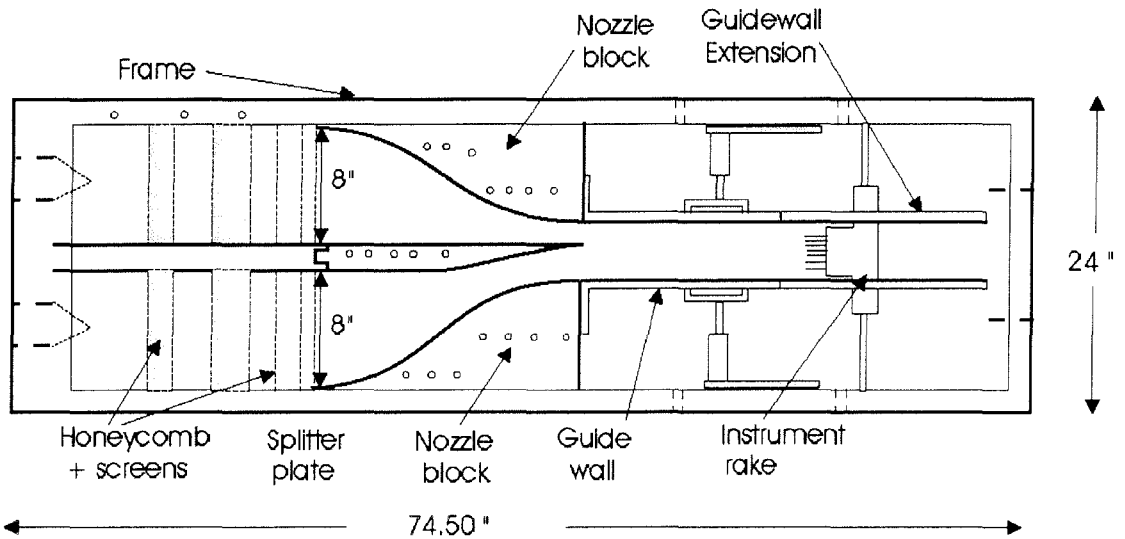

Fig. 2.2: Drawing of the supersonic shear-layer flow-management and test-section regions. Gas flows from left to right (Bond 1998, Fig. 3.3).

Fig. 2.2 shows the supersonic shear-layer flow-management and test-section regions before the installation of the new diffuser system. Coarse-mesh-screen, honeycomb, and a series of fine-mesh-screen sections are used to reduce the turbulence level upstream of the contractions. The two streams are separated in their respective plena by a splitter plate, which is flat on the top (high-speed section) surface and curved on the bottom (low-speed section) surface.

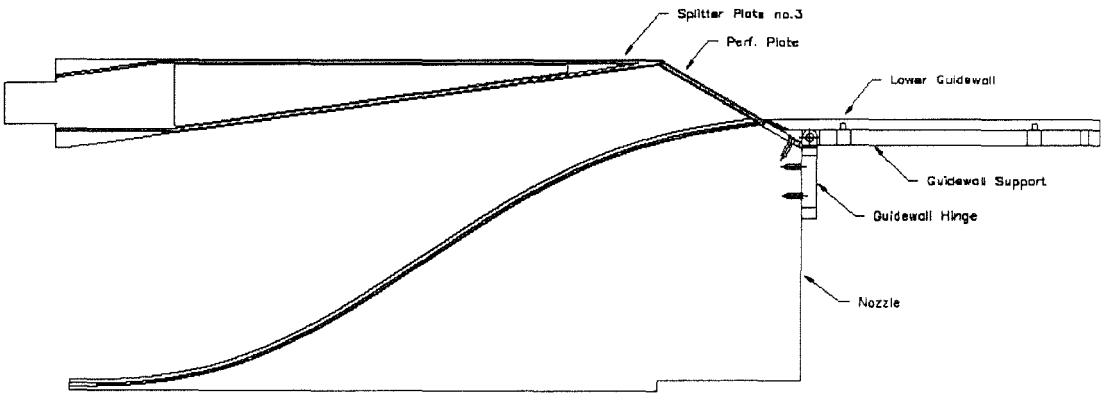

Fig. 2.3: Schematic of the diffuser (Slessor, private communication).

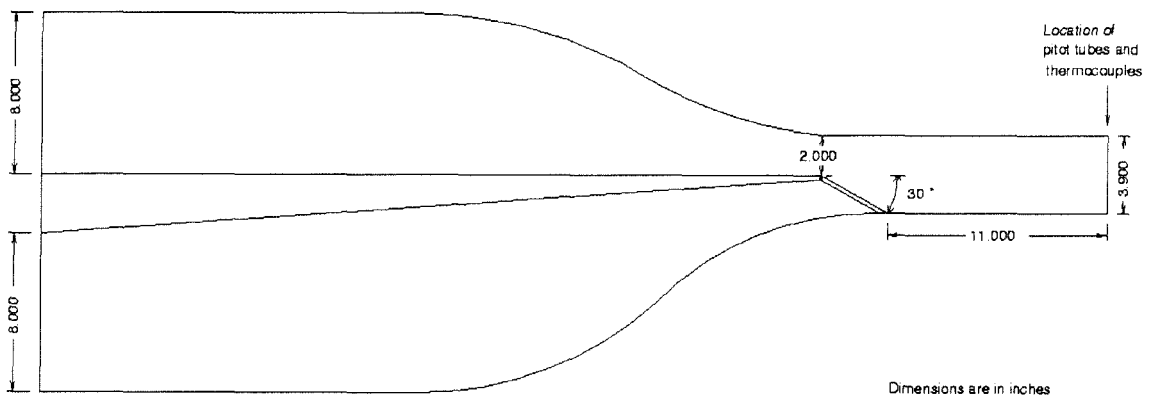

Fig. 2.4: General dimensions of the wind tunnel.

Fig. 2.3 shows the new diffuser design installed in the S^3L Facility. New nozzle, splitter plate, keyway blocks (not shown), lower guidewall components, and an incline ramp were installed in the S^3L Facility. There are two sets of ramps: one that is solid and

the other is perforated. The height of the new nozzle is 8" at the plenum of the nozzle and 2.3" at the exit of the nozzle (Fig. 2.4 shows the general dimension of the wind tunnel). The perforated and non-perforated ramps were designed to have an angle of 30 degrees with respect to the splitter-plate upper surface. The perforated ramp has 3,611 holes, each with a diameter of 0.065" (see Fig. 2.5). The hole pattern open area ratio is approximately 65%, chosen to avoid the jet-coalescence instability (which happens for open-area ratio below 57%) documented by Loehrke and Nagib (1972). The nozzle was designed to maximize flow uniformity and minimize boundary-layer momentum thicknesses at the contraction exit, while ensuring suppression of any flow separation and three-dimensional Taylor-Görtler instabilities. The general dimensions of the new diffuser are shown in Table 2.1. The abbreviations used are indicated in Fig. 1.4.

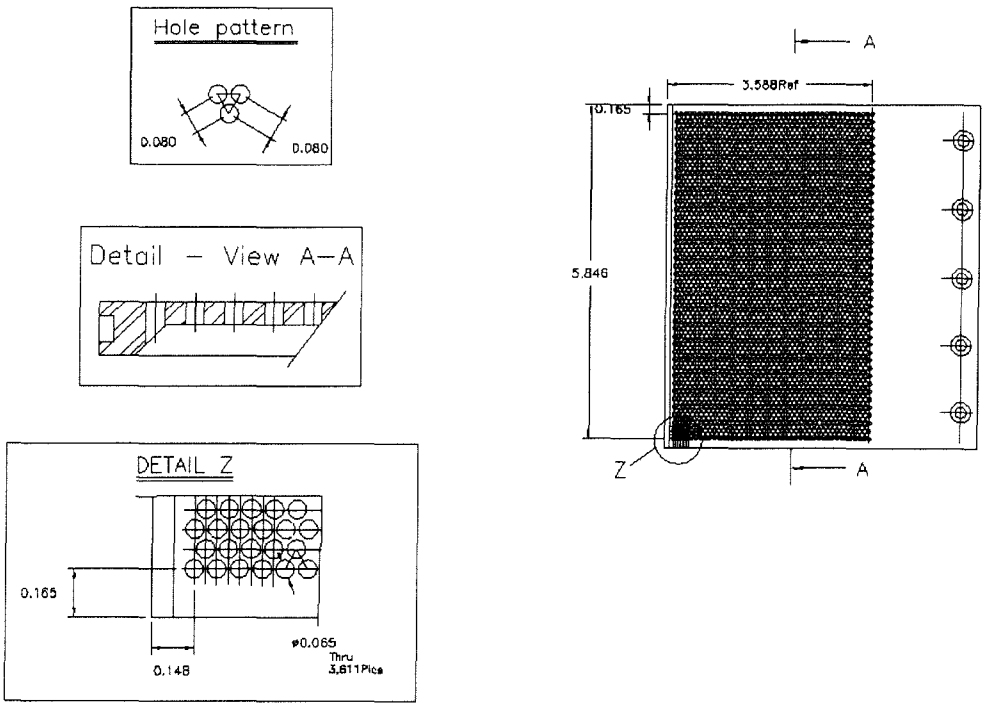

Fig. 2.5: Dimensions of the perforated ramp (Slessor, private communication).

Table 2.1: Dimensions of the current work diffuser.

DESCRIPTION	ABBREVIATION	SIZE
Diffuser angle	2θ	30 degrees
Height	B	6"
Wall Length	N	3.85"
Axial length	L	3.33"
Inlet width	W_1	2"
Exit width	W_2	3.9"
Length ratio	L/W_1	1.665
Aspect ratio	W_2/W_1	1.95
Aspect ratio	B/W_1	3

2.2 S^3L low-speed-valve calibration

With the installation of the new nozzle and ramp, S^3L required recalibration of the micrometer valve for the low-speed section. All calibrations were done using N_2, with the tank pressure at 652,934 Pa. Static pressure probe was installed at the upstream of the nozzle (referred as Station 1 in this section). A total of 10 micrometer settings were measured with and without the perforated ramp installed.

First, the static pressure was measured without the ramp at 10 different micrometer settings. Knowing the pressure at Station 1, the nozzle area ratio, the atmospheric pressure (99000 Pa for a density of 1.16 Kg/m^3), and assuming at the exit of the nozzle (referred as Station 2 in this section) the static pressure is same as atmospheric pressure, we could find the velocity at Stations 1 and 2 using Bernoulli's equation (Eq. 2.1) and the conservation-of-mass equation (Eq. 2.2):

$$U_{2a} = \sqrt{\frac{2\cdot(Ps_{1a} - Ps_{2a})}{\rho_2 - \frac{\rho_2^{\,2}}{\rho_1}\cdot\left(\frac{h_2}{h_1}\right)^2}} \tag{2.1}$$

$$U_{1a} = \frac{U_{2a} \cdot h_2}{h_1}, \tag{2.2}$$

where, U is the velocity, Ps is the static pressure, ρ is the density, and h is the height of the nozzle. Subscript "*1*" is at the station upstream of the nozzle, "*2*" is at the end (downstream) of the nozzle, "*a*" is without the ramp, and "*b*" is with the ramp installed. Fig. 2.6 shows the velocity calibration without the ramp.

With the perforated ramp installed, the static pressure measurement was repeated at Station 1 with the same micrometer setting and tank pressure. Therefore, the density at Station 1 with the ramp installed was calculated using the isentropic-flow relation (Eq. 2.3):

$$\rho_{1b} = \left(\frac{P_{1b}}{P_{1a}}\right)^{\frac{1}{\gamma}} \cdot \rho_{1a} \tag{2.3}$$

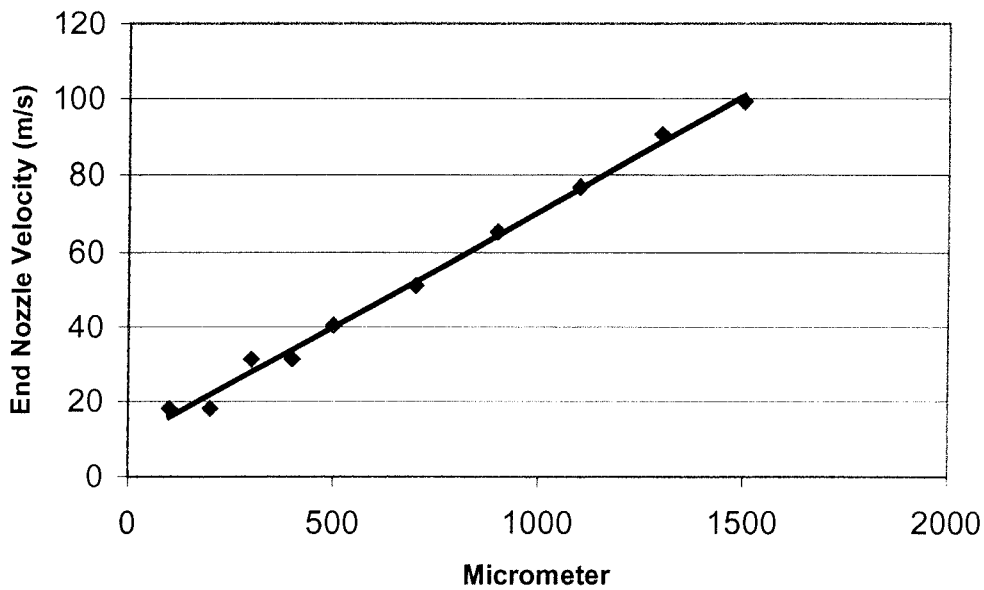

Fig. 2.6: Micrometer setting vs. end of nozzle velocity, no ramp (End of NozzleVelocity = 0.0607 x Micrometer + 9.7552).

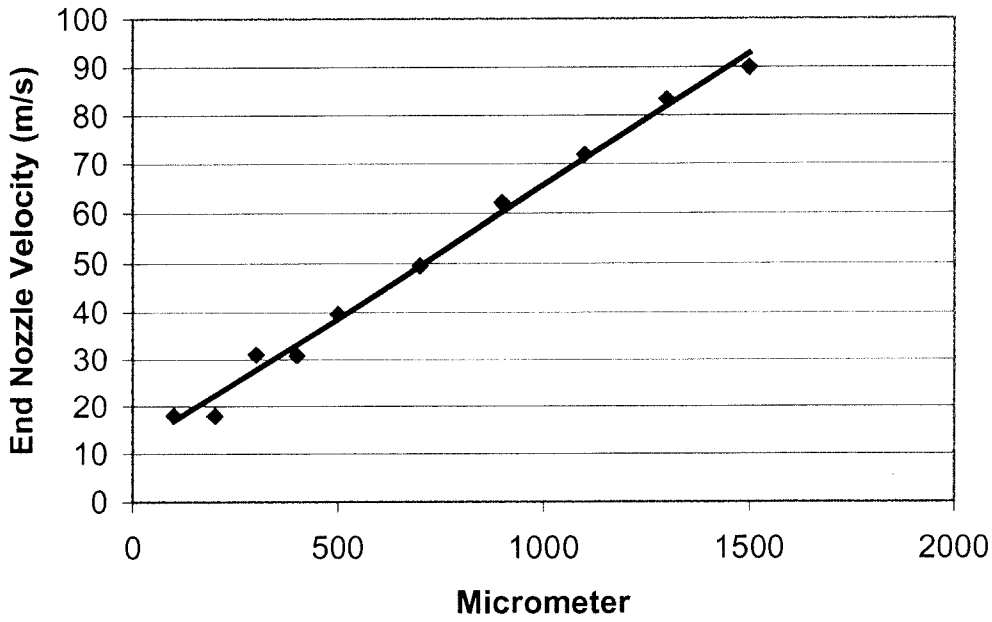

Fig. 2.7: Micrometer setting vs. end nozzle velocity, ramp (End of NozzleVelocity = 0.0541 x Micrometer + 11.576).

Since the nozzle is sonic, the mass flow rate for both, with and without the perforated ramp, is fixed by the micrometer setting, tank pressure, and type of gas. This is true if the plenum pressure after the micrometer valve is lower than ~50% of the tank pressure so as to ensure sonic operation. Using continuity (Eq. 2.4), the velocity at Station 1 with the ramp installed was obtained:

$$U_{1b} = \frac{\rho_{1a} \cdot U_{1a}}{\rho_{1b}} \tag{2.4}$$

Then, using conservation of mass, the velocity at the end of the nozzle was calculated (see Fig. 2.7).

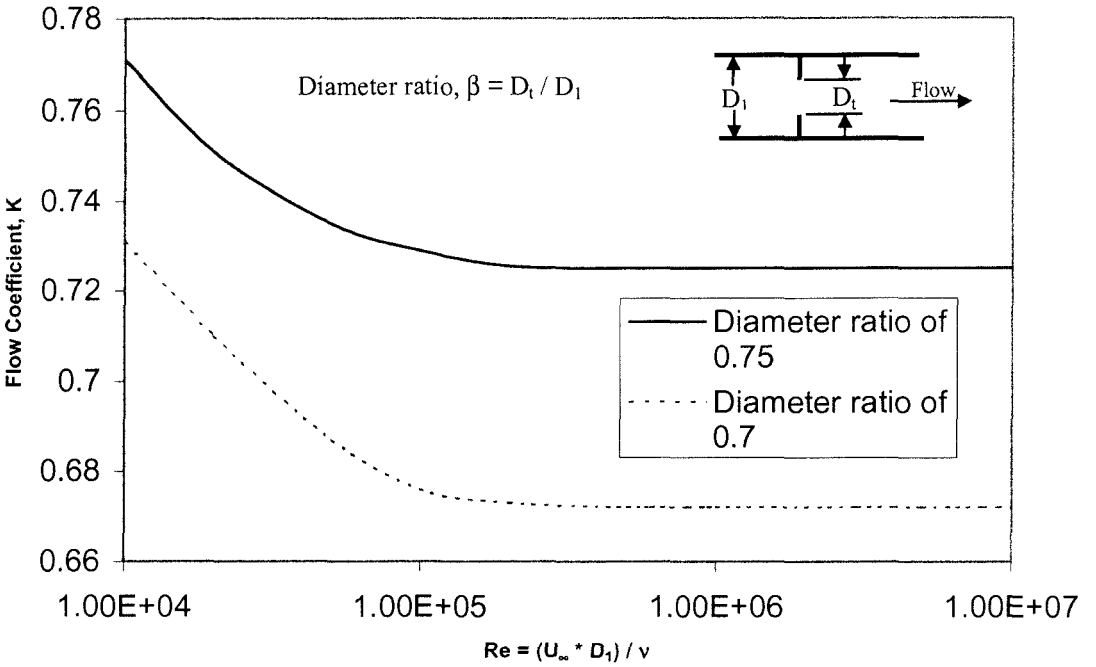

Fig. 2.8: Flow coefficients for concentric orifices with corner taps (Fox and McDonald 1992, and Miller 1985).

Static pressure at Station 2 with the ramp was calculated using Bernoulli's equation. This pressure rise could be predicted using an orifice-plate model. Using Fig. 2.8 (Fox and McDonald 1992, and Miller 1985), the diameter ratio or square-root of the area ratio of the ramp is defined as

$$\beta = \frac{D_t}{D_1} = \sqrt{\frac{A_t}{A_1}}, \tag{2.5}$$

where β is the diameter ratio or square-root of the area ratio, D is the diameter in a pipe, A is the area, subscribe "t" is for throat or hole, and "1" is for total diameter of the pipe or area of the diffuser surface. Knowing β for the ramp (which is 0.72 for the facility), one can obtain the flow coefficient, K, at high Reynolds number, to be 0.7. Since the mass flow rate was constant at a given micrometer setting, the flow coefficient from the calibration was calculated using Eq. 2.5:

$$K = \frac{m}{A_t \cdot \sqrt{2 \cdot \rho_{2b} \cdot (P_{2b} - P_{atm})}}, \tag{2.6}$$

where, K is the flow coefficient, and m is the mass flow rate.

At high Reynolds number (high micrometer setting), the highest experimental flow coefficient was around 0.67. The small flow coefficient difference between the experimental results compared with previous work shown in Fig. 2.9 (Fox and McDonald 1992, and Miller 1985) maybe because the previous work was based on one-hole concentric orifice opening instead of multiple-hole orifices.

2.3 Method, instrumentation, and diagnostics

Two types of experimental results will be documented here: Schlieren visualizations and mean-pressure measurements. Although the data-acquisition system also recorded mean-temperature measurements, these data were not used. Schlieren visualization records instantaneous spanwise-averaged structure in the layer, indicating the mixing regions, and whether shear-layer growth is linear. Fig. 2.9 shows the schematic of the Schlieren visualization system. Schlieren visualizations were recorded with a 1024^2-pixel, 30 fps CCD camera by Silicon Mountain Design, Model SMD 1M30. It uses a Xenon Corp. N-789B nanolamp capable of maintaining light source for 20 ns.

Velocity profiles downstream of the diffuser were recorded using the total mean-pressure measurements (the location of the rakes is shown in Fig. 2.4) and static mean-pressure measurements. There are two static probes, one at the end of the high-speed nozzle, and the other above the rake (both are in upper guidewall). The atmospheric temperature and pressure were measured just before each experimental run. Knowing these data and using an isentropic flow relation, one can deduce the velocity profile. Slessor (1998) has a more detailed description of the data-acquisition system.

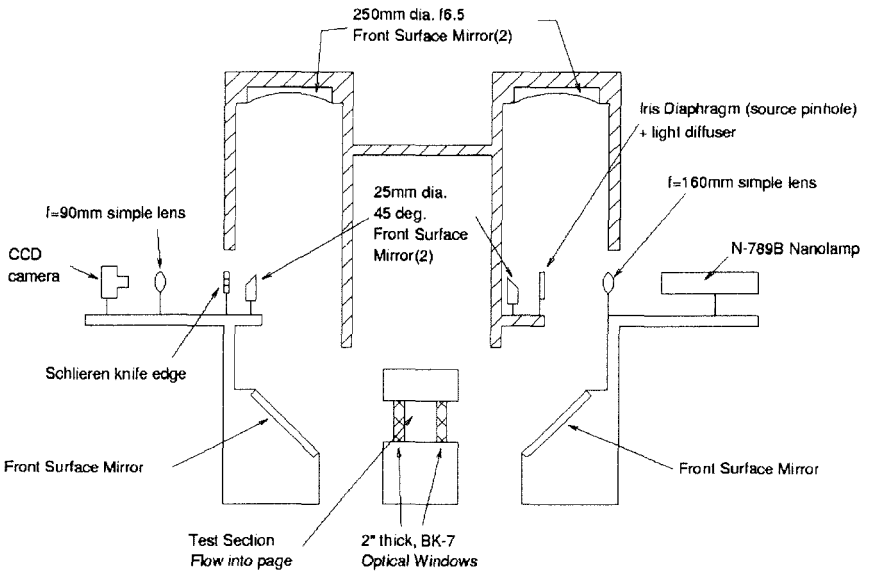

Fig. 2.9: Schematic of Schlieren visualization system.

2.4 Error bar and least-square fits

Figures from following sections will show error bars and least-square fit lines. Error bars were based on the standard deviation equation:

$$\delta\langle x\rangle = \sqrt{\frac{1}{N\cdot(N-1)}\cdot\sum_i\left(x_i-\langle x\rangle\right)^2} \tag{2.7}$$

$$\langle x\rangle = \frac{1}{N}\cdot\sum_i x_i\,, \tag{2.8}$$

where $\delta\langle x\rangle$ is the standard deviation, N is the number of samples, x_i is the individual value measured at each sample, and $\langle x\rangle$ is the average value.

Since the length of the experimental tests varied from 2 to 6 seconds, data analyzed take only a fraction of this time, over which the flow in the facility has reached a steady-state condition. The data acquired from this fraction is then segmented, averaged, and the standard deviations calculated.

Least-square fit lines were calculated using the following equation:

$$LSF = \sum_i \frac{(y(x) - y_i)^2}{\delta\langle x \rangle^2}, \tag{2.9}$$

where $y(x)$ is the polynomial equation used to fit the data, and y_i is the individual data value. To find the polynomial equation that best fits the data, the least-square fit is minimized, solving for the coefficients of the polynomial.

CHAPTER 3

Top-stream flow only

The first set of experiments was conducted with the perforated plate replaced by a solid ramp to determine the reference behavior of the flow with no mass injection. The high-speed section (top-stream flow) was run at different speeds using N_2.

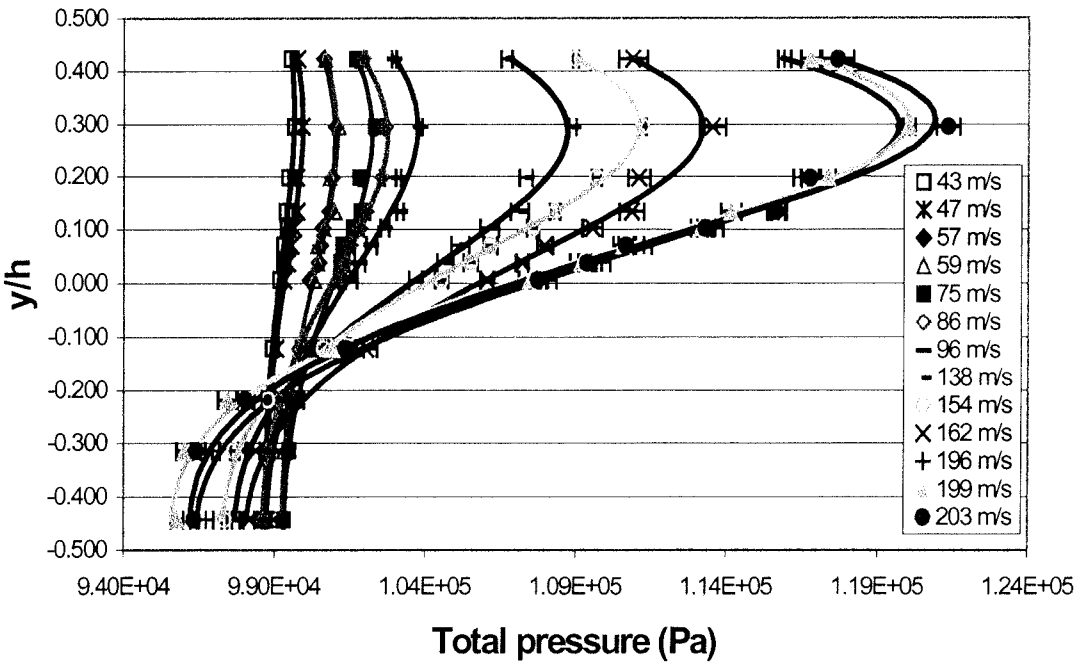

Fig. 3.1: Total pressure profile (top-stream flow only).

Fig. 3.1 shows the total pressure profiles obtained at the location of the rake. The velocity shown in the legend is the maximum velocity achieved for that particular run. If the static pressure located at the top of the rake is used, the normalized velocity profile for different maximum freestream velocities can be calculated, and is shown in Fig. 3.2. *h* is the total height of the test section, which is 3.9". The least-square fit lines in Fig. 3.2 were based on a third-order polynomial. The least-square fit lines in Fig. 3.1 were based

on the third-order polynomial least-square-fit equation from the normalized velocity profiles in Fig. 3.2. As can be seen from the normalized velocity profiles, as the freestream velocity increases, the reattachment point of the separation bubble moves further downstream. Fig. 3.3 depicts the flow geometry as the velocity varies, for top-stream flow only. As velocity increases, the boundary-layers in the top-guidewall and the splitter plate are reduced, and the reattachment point of the separation bubble (stall transition flow) increases, which is why the normalized velocity profiles have that shape at different velocities.

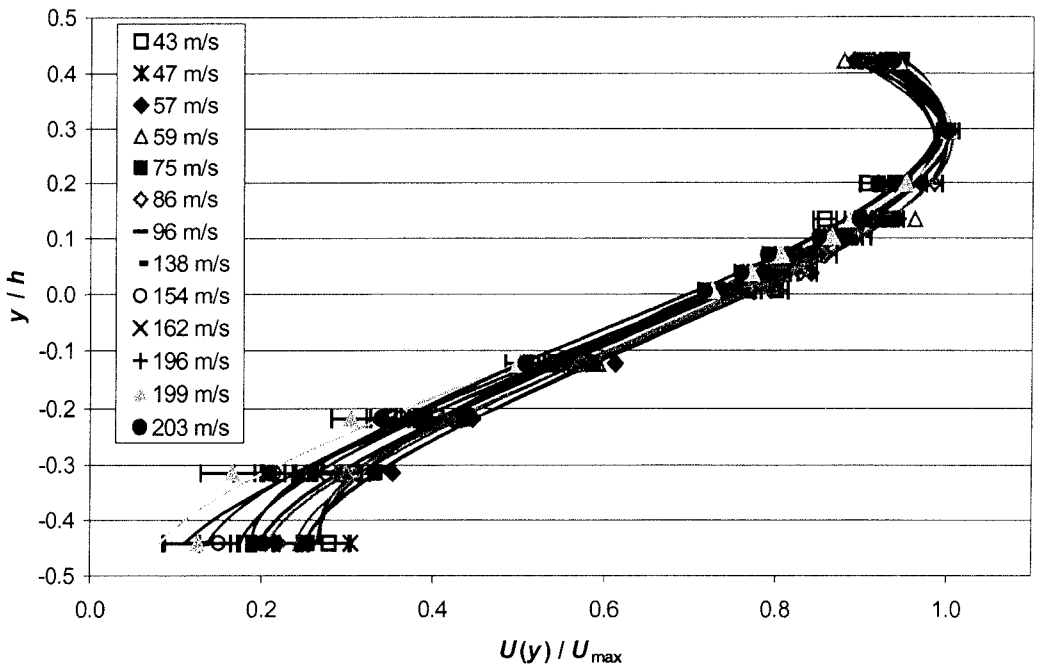

Fig. 3.2: Normalized velocity profile (top-stream flow only).

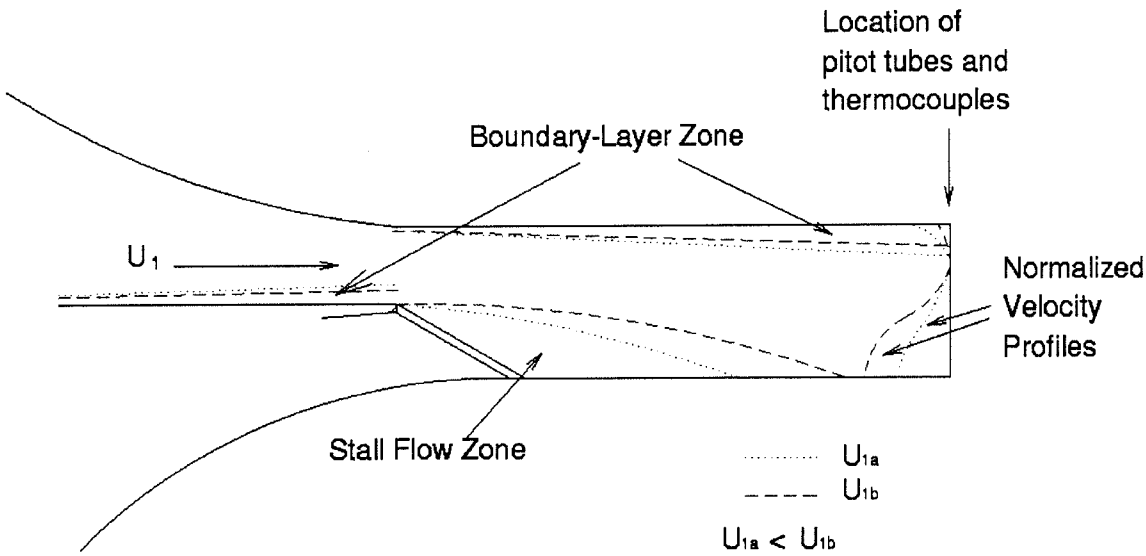

Fig. 3.3: Flow geometry at different top-stream flow velocities.

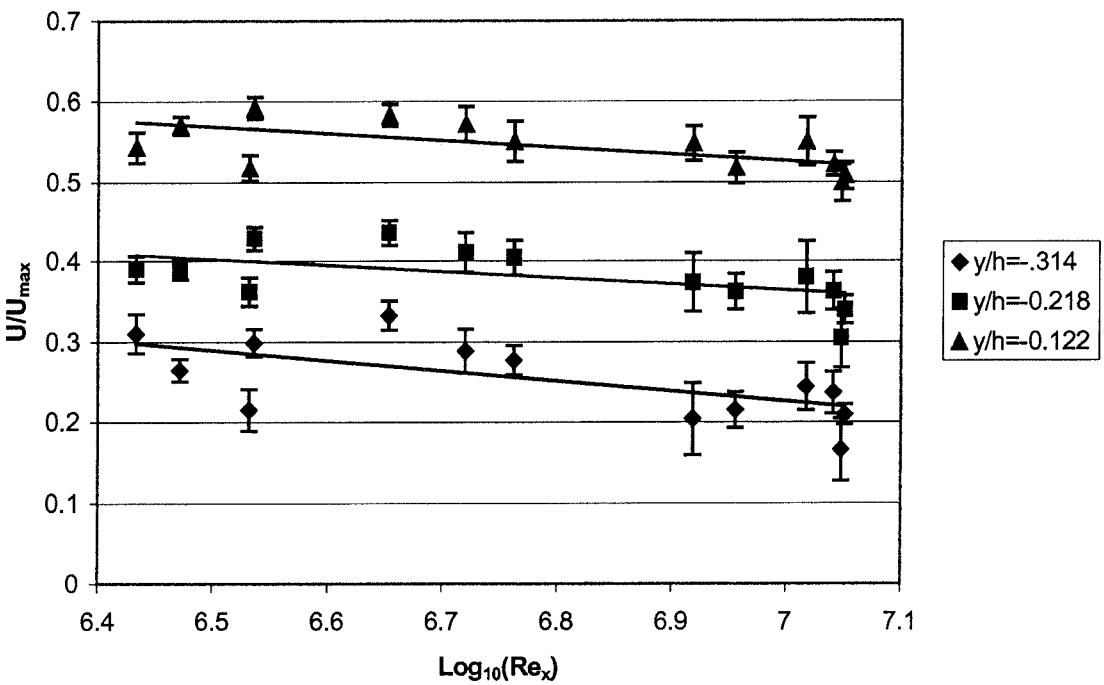

Fig. 3.4: Normalized velocity at fixed height.

Fig. 3.4 shows a detailed analysis of the reattachment of the separation bubble. The figure shows the normalized velocity at the fixed measuring station versus upstream

Reynolds number for the three lowest pitot pressure probes in the test section. This plot suggests that the location of the reattachment point for this flow varies weakly with Reynolds number. This is not in accord with the conclusion in Song, DeGraaff, and Eaton (2000) who reported that the reattachment point of the separation bubble is independent of Reynolds number. Although Song, DeGraaff, and Eaton's (2000) experiment was based on a contoured diffuser, their conclusion was that the separation point of the separation bubble was different but the reattachment point was the same.

A redundancy check on the measurement system can be performed by calculating the velocity at the high-speed nozzle exit, U_1. For example, for the U_{max} = 47 m/s run, integrating the velocity profile shown in Fig. 3.2 and using the conservation of mass, U_1 is calculated to be 53 m/s. The other measurement system yields the static pressure at the upstream of the nozzle and at the exit of the nozzle, by using conservation of mass and the momentum equation, U_1 is calculated to be 57 m/s. The difference between these velocities is probably attributable to unaccounted boundary-layer contributions.

CHAPTER 4

Two-stream flow

4.1 Two-stream flow at the same density ratio

Experiments were performed with injection of a density-matched helium/argon (2/3 argon and 1/3 helium) mixture (for low-speed section) into an upper, high-speed stream of nitrogen. Nitrogen was used because it is inexpensive. Helium was used because its index of refraction is lower than that of nitrogen (therefore, a better Schlieren effect) and argon was used for density matching.

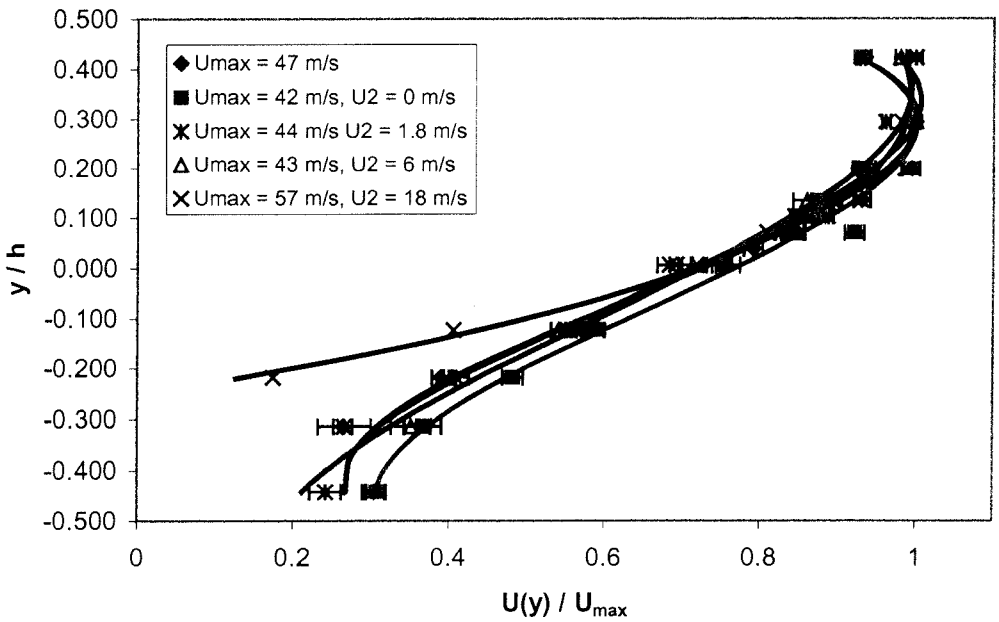

Fig. 4.1: Normalized streamwise velocity profiles for mass injection of a density-matched mixture (N_2 and Ar/He) for $U_1 \cong 57$ m/s.

Fig. 4.1 plots the normalized velocity profile for various levels of mass injection of a density-matched He/Ar mixture into the upper, N_2 stream. The velocity at the high-speed nozzle exit was held constant ($U_1 \cong 57$ m/s). The legend for Fig. 4.1 shows the maximum velocity attained, U_{max}, at the location of the rake. U_2 is the velocity at the low-

speed nozzle exit (just before the perforated ramp). The run with U_{max} = 47 m/s was performed with no mass injection (solid inclined surface) and compared to the run U_{max} = 42 m/s and U_2 = 0 m/s with the same upstream velocity, but with the small mass injection derived from the initial volume of gas in the low-speed plenum (initially at a slightly higher pressure). Subsequent runs were performed with mass injection from the low-speed stream at velocities of 1.8, 6.0, and 18 m/s, respectively. As expected and inferred from these data, the reattachment point moves downstream as mass injection increases (see Fig. 4.2). Although Fig. 4.2 shows how the flow behaves with no mass injection, compared with mass injection at low-speed section, the same behavior can be applied as mass injection in the low-speed section increases.

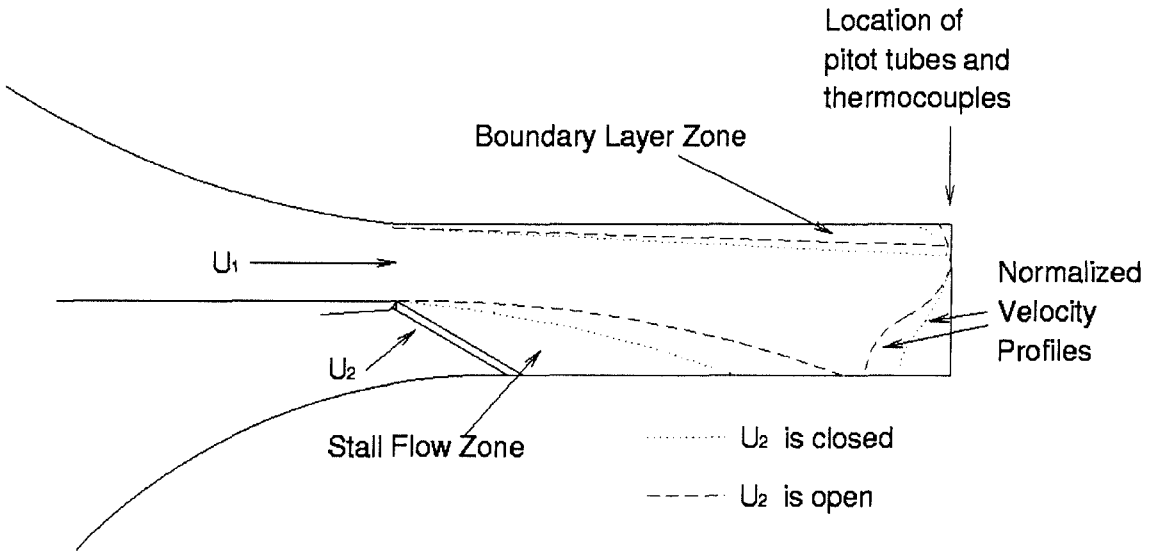

Fig. 4.2: Flow geometry at constant high-speed velocity (U_1) varying low-speed velocity (U_2).

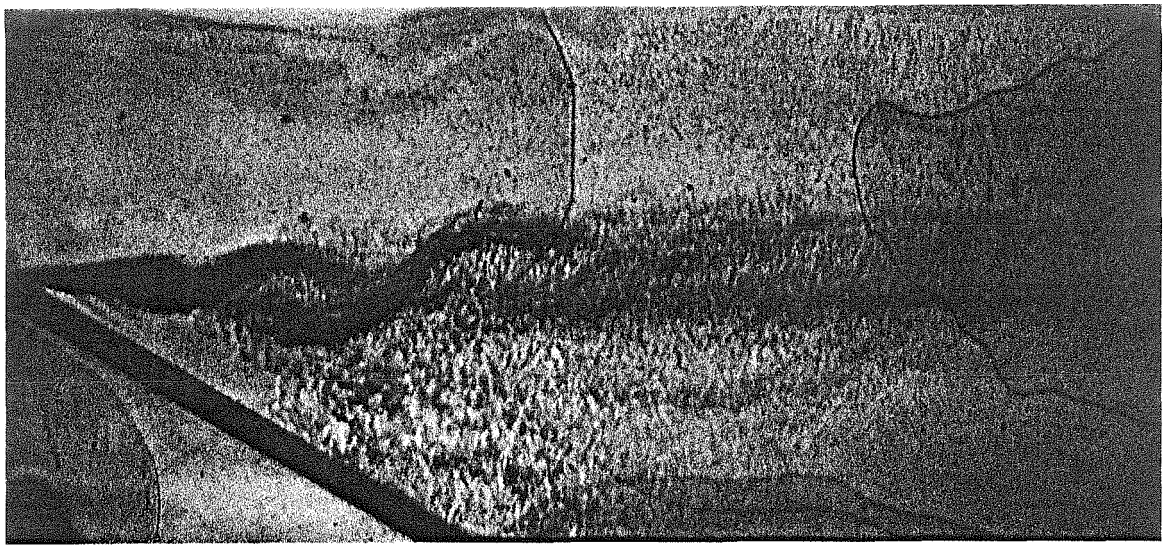

Fig. 4.3: Schlieren visualization after expansion turn; $U_1 \cong 57$ m/s [N_2] and $U_2 \cong 1.8$ m/s [He/Ar].

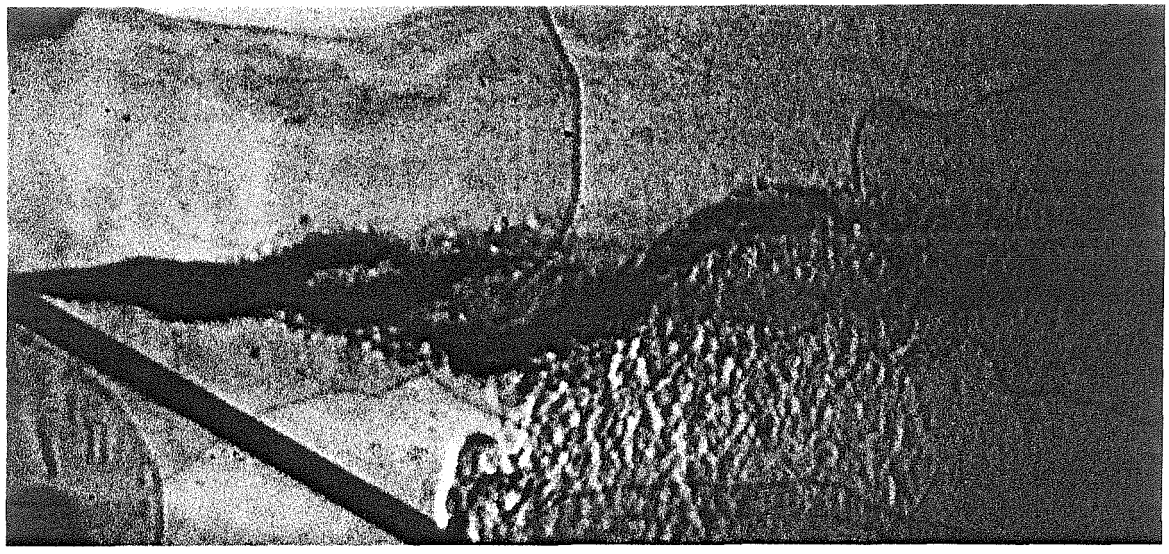

Fig. 4.4: Schlieren visualization after expansion turn; $U_1 \cong 57$ m/s [N_2] and $U_2 \cong 6$ m/s [He/Ar].

Figs. 4.3 and 4.4 show the Schlieren visualization of the upstream flow with $U_1 \cong$ 57 m/s, and $U_2 \cong 1.8$ m/s and 6 m/s, respectively. In these figures, a small region of uniformly mixed fluid is discernible, just downstream of the perforated plate, with a recirculation zone downstream of this region. Fig. 4.5 shows a schematic of the geometry and flow zones that describe the previous Schlieren visualizations figures. There is an

unmixed region (region I in Fig. 4.5) that increases as U_2 increases, as shown in Fig. 4.3 and 4.4. The mixing region or the separation (transition stall) bubble (region II in Fig. 4.5) increases as U_2 increases. The Schlieren visualization system was able to record 30 frames per second. The sequence of pictures was converted to a movie and shows that the separation bubble was slightly unstable; therefore, the reattachment point of the separation bubble was slightly unstable also. Another observation from Fig. 4.1 is that as U_2 increases, the size of the boundary-layer at the top guidewall of the test section (region IV in Fig. 4.5) decreases.

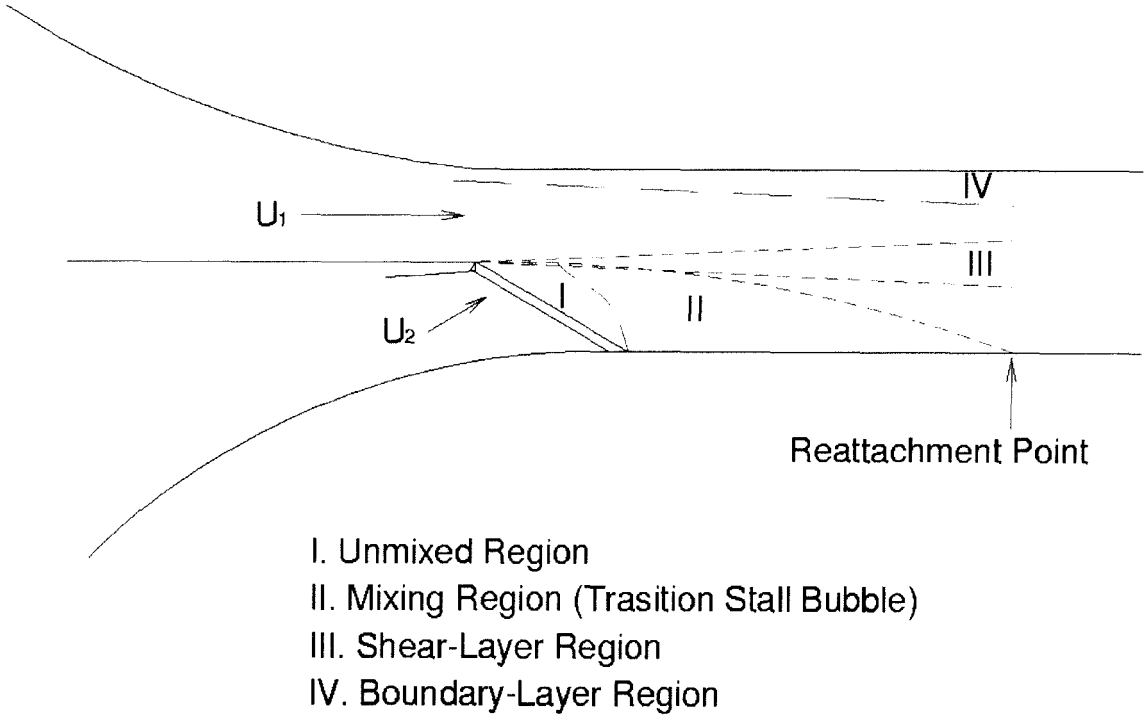

Fig. 4.5: Geometry and flow zones of two-stream flow diffuser.

Fig. 4.6 is a composite of two runs performed with the same inflow (since the field of view of the Schlieren visualization system was not big enough to fit the entire test section), $U_1 \cong 57$ m/s and $U_2 \cong 18$ m/s, one with the upstream region, the other with the downstream region. In this last figure, the transition from a separated region towards a classical shear layer is apparent, with a separated-flow region reattachment beyond the measuring station that is apparent from the plots in Fig. 4.1.

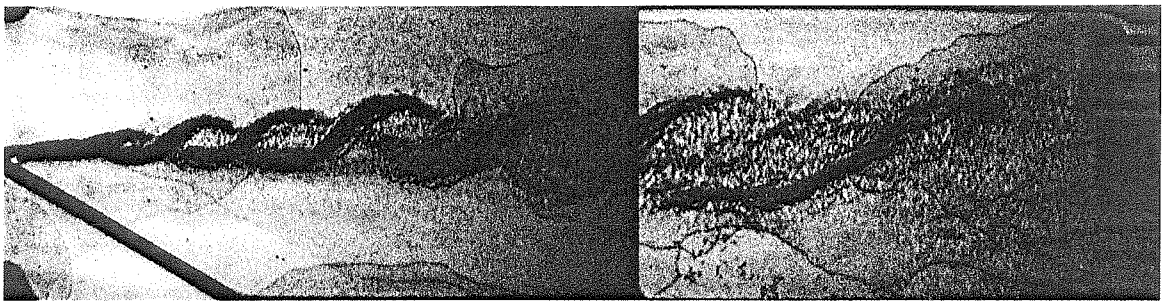

Fig. 4.6: Schlieren visualization after expansion turn; $U_1 \cong 57$ m/s [N_2] and $U_2 \cong 18$ m/s [He/Ar].

4.2 Two-stream flow at the same density ratio at higher speed

Another set of experiments was performed by increasing the speed of the flow but keeping approximately same the velocity ratio ($r = U_2/U_1$) and the same density ratio as in the experiments described in Chapter 4.1.

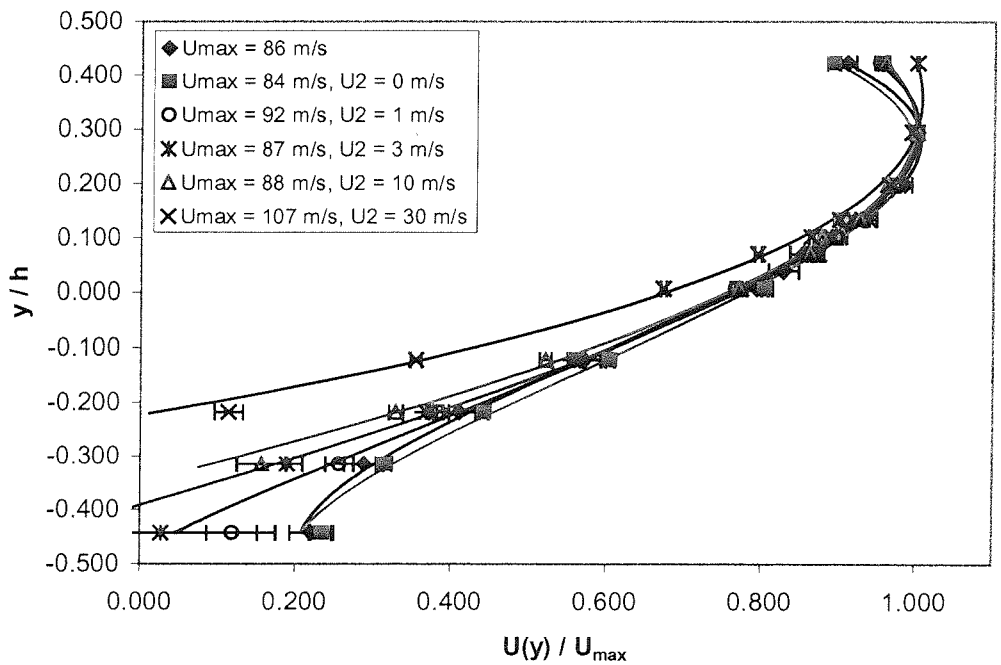

Fig. 4.7: Normalized streamwise velocity profiles for mass injection of a density-matched mixture (N_2 and Ar/He) for $U_1 \cong 92$ m/s.

Fig. 4.7 shows the normalized velocity profiles for various levels of mass injection of a density-matched He/Ar mixture into the upper, N_2 stream. The velocity at the high-speed nozzle exit was held constant ($U_1 \cong 92$ m/s). The run with $U_{max} = 86$ m/s was performed with no mass injection (solid inclined surface), and compared to the run $U_{max} = 84$ m/s and $U_2 = 0$ m/s with the same upstream velocity, but with the small mass injection derived from the initial volume of gas in the low-speed plenum (initially at a slightly higher pressure). Subsequent runs were performed with mass injection in the low-speed stream at velocities of 1, 3, 10, and 30 m/s, respectively. Again, as expected and inferred from these data, the reattachment point moves downstream as the mass injection rate is increased (see Fig. 4.2).

Comparing with the results in section 4.1 (Fig. 4.1 with Fig. 4.7), a set of figures was plotted. Figs. 4.8, 4.9, and 4.10 show the normalized streamwise velocity profiles for mass injection of a density-matched mixture for $U_2/U_1 \cong 0.032$, 0.107, and 0.321, respectively. From these plots, one can see that while keeping the same velocity ratio, if the overall speed is higher, the reattachment point of separation bubble increases.

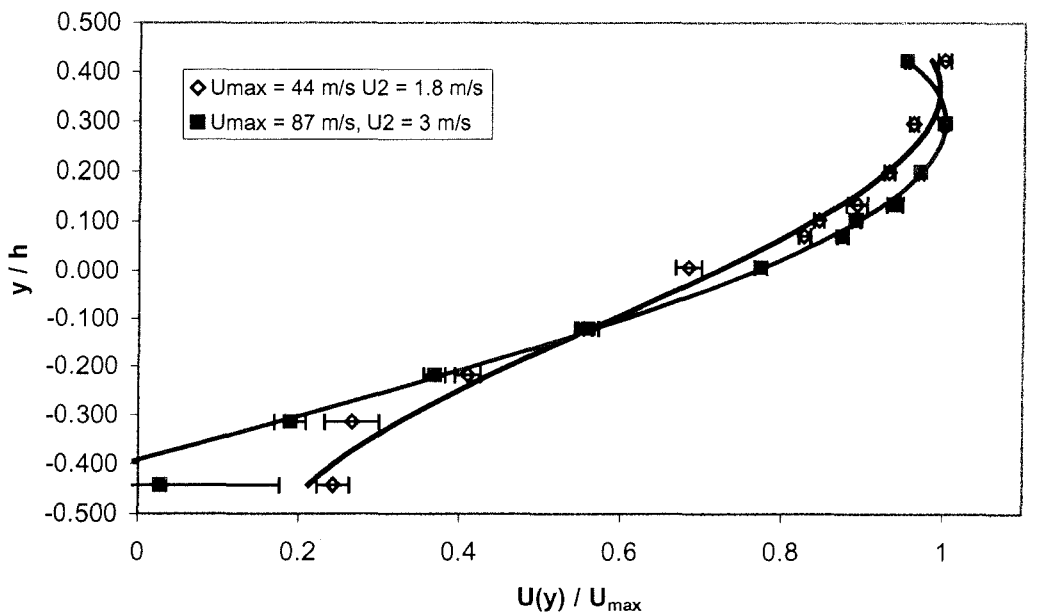

Fig. 4.8: Normalized streamwise velocity profiles for mass injection of a density-matched mixture (N_2 and Ar/He) for $U_2/U_1 \cong 0.032$.

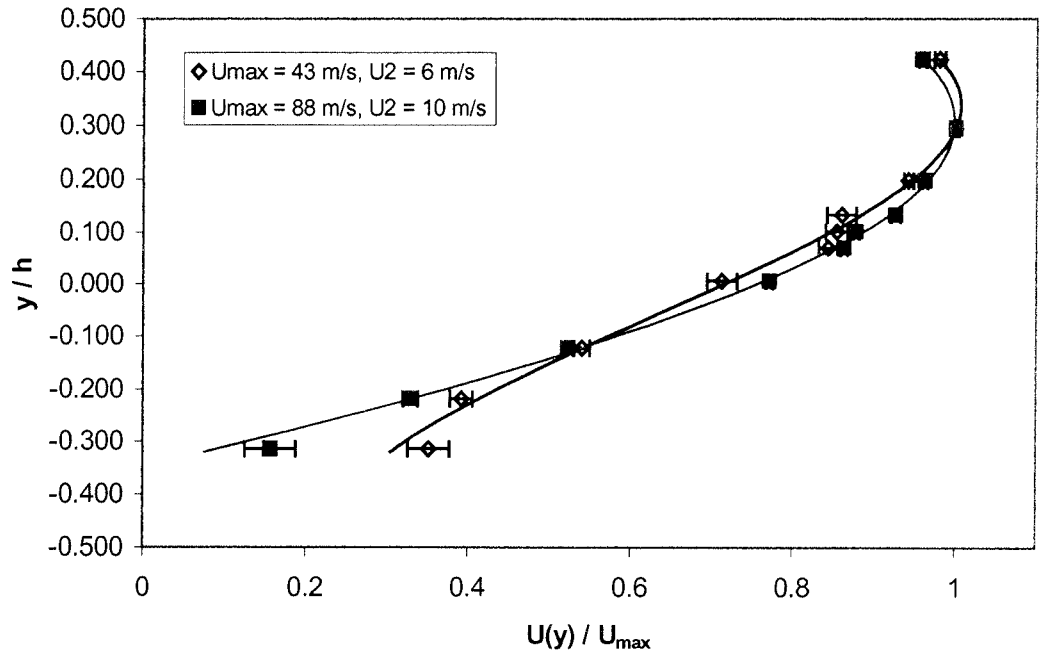

Fig. 4.9: Normalized streamwise velocity profiles for mass injection of a density-matched mixture (N_2 and Ar/He) for $U_2/U_1 \cong 0.107$.

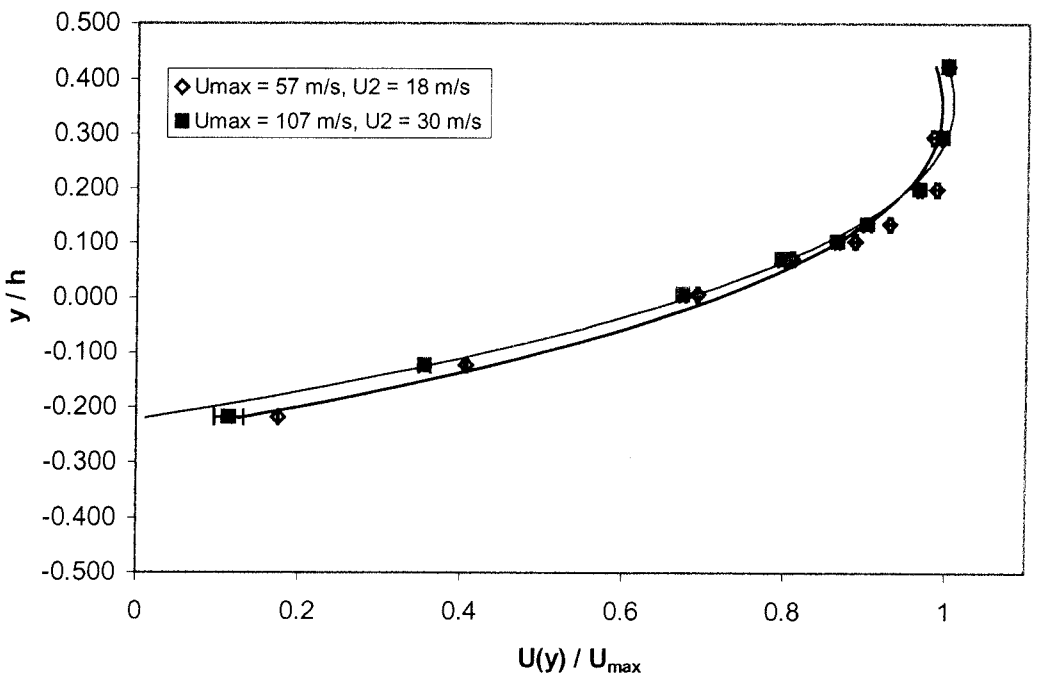

Fig. 4.10: Normalized streamwise velocity profiles for mass injection of a density-matched mixture (N_2 and Ar/He) for $U_2/U_1 \cong 0.321$.

Schlieren visualizations in Figs. 4.11, 4.12, and 4.13 show the upstream flow with $U_1 \cong 92$ m/s, and $U_2 \cong 1$, 3, and 10 m/s, respectively. The small region of unmixed fluid is discernible again, just downstream of the perforated plate, with a recirculation zone downstream of this region. The non-mixing region (region I in Fig. 4.5) increases as U_2 increases, as shown previously in Chapter 4.1. The mixing region or the separation (transition stall) bubble (region II in Fig. 4.5) increases as U_2 increases. Fig. 4.7 shows that as U_2 increases, the size of the boundary-layer at the top guidewall of test section (region IV in Fig. 4.5) decreases.

Fig. 4.11: Schlieren visualization after expansion turn; $U_1 \cong 92$ m/s [N_2] and $U_2 \cong 1$ m/s [He/Ar].

Fig. 4.12: Schlieren visualization after expansion turn; $U_1 \cong 92$ m/s [N_2] and $U_2 \cong 3$ m/s [He/Ar].

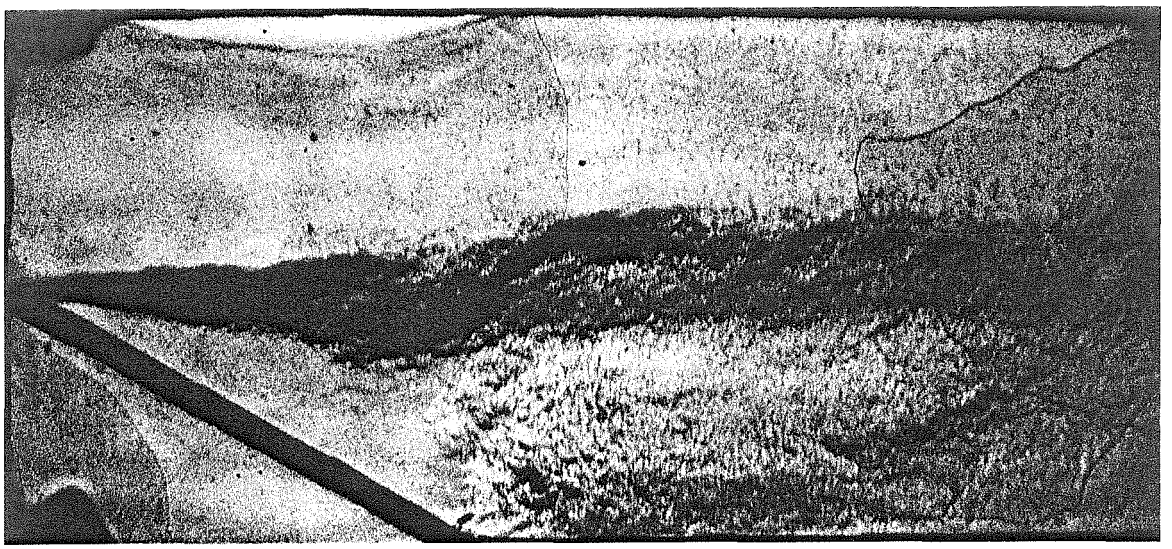

Fig. 4.13: Schlieren visualization after expansion turn; $U_1 \cong 92$ m/s [N_2] and $U_2 \cong 10$ m/s [He/Ar].

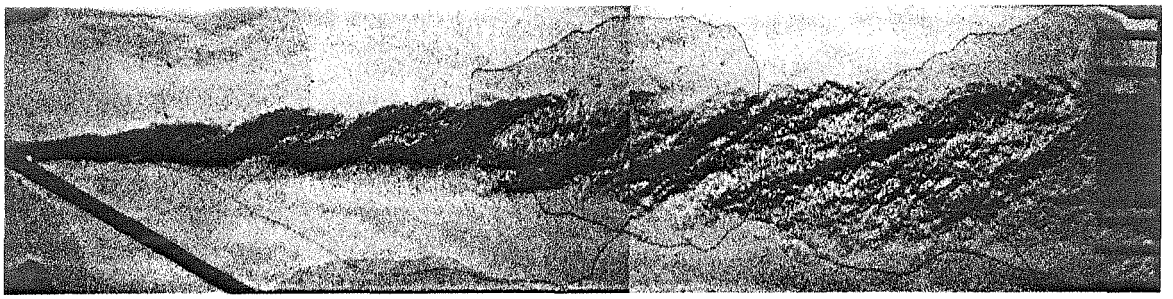

Fig. 4.14: Schlieren visualization after expansion turn; $U_1 \cong 92$ m/s [N_2] and $U_2 \cong 30$ m/s [He/Ar].

Fig. 4.14 is a composite of two runs performed with the same inflow, $U_1 \cong 92$ m/s and $U_2 \cong 30$ m/s, one with the upstream region, the other with the downstream region. The transition from a separated region towards a classical shear layer is apparent again, with a separated-flow region reattachment beyond the measuring station that is apparent from the plots in Fig. 4.7. Comparing Fig. 4.14 with 4.6 (both with same velocity ratio and density-matched ratio), the shear layer growth for Fig. 4.14 (higher speed) is smaller than Fig. 4.6 (therefore the separation bubble for the higher velocity is slightly bigger). This agrees with the result in Fig. 4.10, in which the reattachment point is slightly further downstream for the higher speed flow.

4.3 Coefficient of pressure for two-stream flow at the same density ratio

Many aspects of diffuser operation can be parameterized in terms of a pressure coefficient,

$$C_p = \frac{p_2 - p_1}{\frac{1}{2}\rho(U_1)^2}. \tag{4.1}$$

This is plotted in Fig. 4.15, with Point 1 located on the top guidewall, above the starting point of the ramp, and Point 2, also on the top guidewall, at the downstream location of the total-pressure-probe array. The data points at $U_2 = 0$ correspond to flow with no mass injection. As expected, the pressure coefficient decreases with increasing mass injection, as the reattachment point is pushed further downstream and the flow evolves to form a classical shear layer with a small streamwise pressure gradient (*e.g.*, Dimotakis 1991).

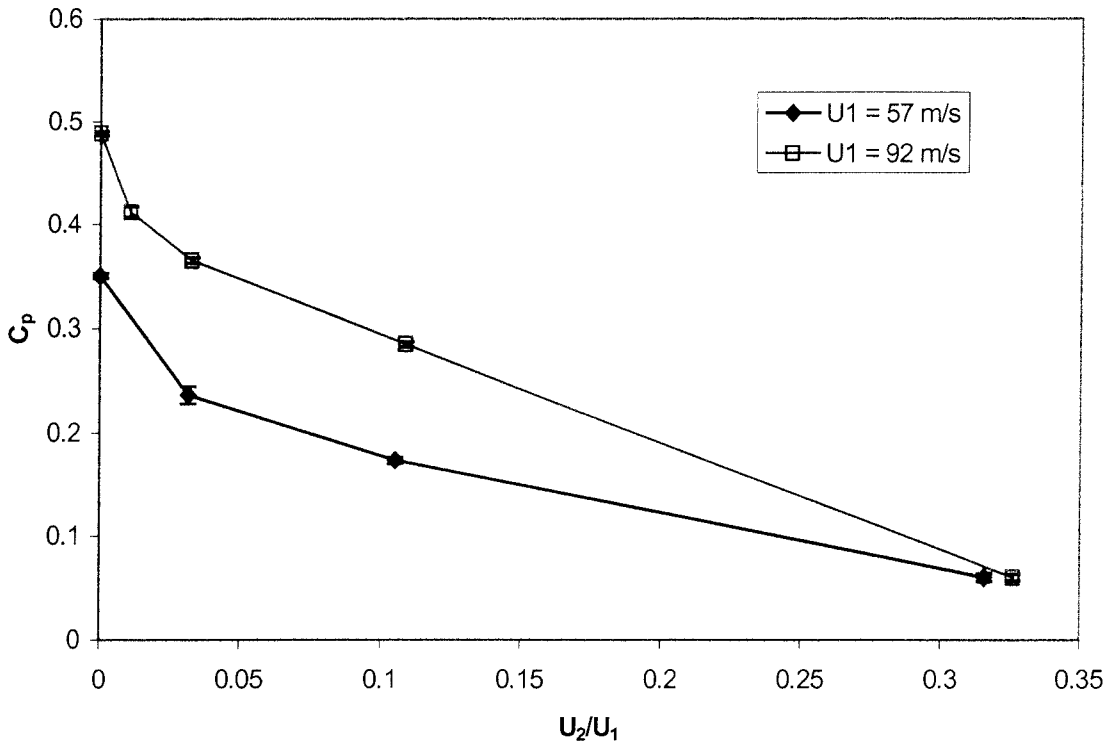

Fig. 4.15: Internal-flow pressure coefficient as function of mass-injection speed of a density-matched mixture (N_2 and Ar/He).

4.4 Two-stream flow for higher density ratio

Experiments were then performed with injection of pure argon for low-speed section and pure nitrogen for high-speed section. The density ratio is: $s = \rho_2/\rho_1 = 1.43$ (ρ_1 is the density for high-speed section and ρ_2 is for low-speed section). Velocities for both high-speed section (U_1) and low-speed section (U_2) were the same as for the density-matched set of experiments documented in Chapter 4.1.

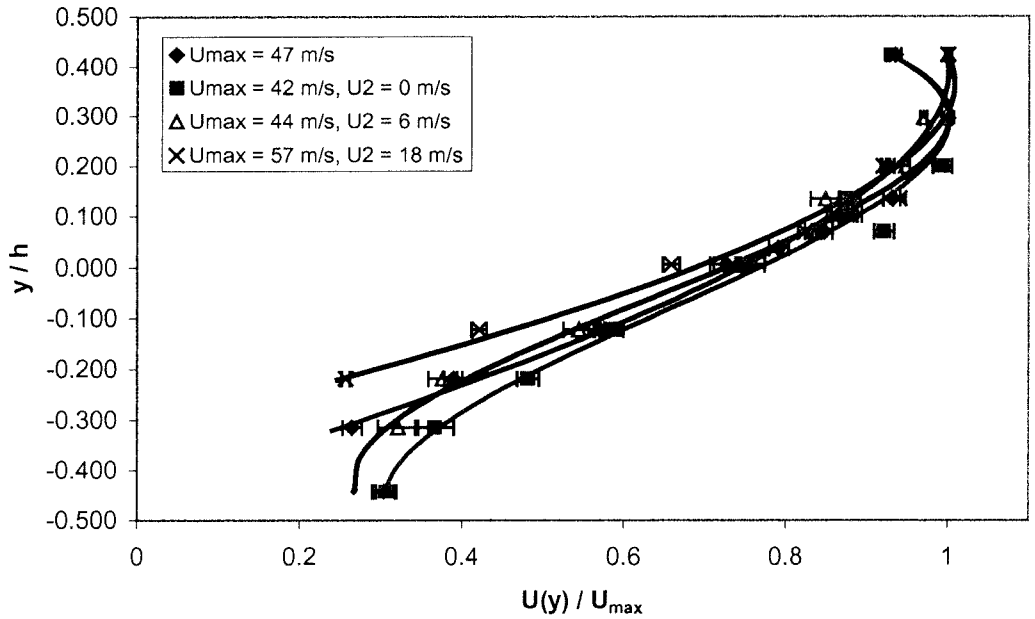

Fig. 4.16: Normalized streamwise velocity profiles for mass injection of a density ratio of 1.43 (N_2 and Ar) for $U_1 \cong 57$ m/s.

Fig. 4.16 plots the normalized velocity profile for various levels of mass injection at a density ratio of 1.43 (N_2 in high-speed section and Ar in low-speed section). The velocity at the high-speed nozzle exit was held constant, with the same velocity as the runs in chapter 4.1 ($U_1 \cong 57$ m/s). The run with $U_{max} = 47$ m/s was performed with no mass injection (solid inclined surface) and compared to the run $U_{max} = 42$ m/s and $U_2 = 0$ m/s with the same upstream velocity, but with the small mass injection derived from the initial volume of gas in the low-speed plenum (initially at a slightly higher pressure). Subsequent runs were performed with mass injection from the low-speed stream at

velocities of 6 and 18 m/s, respectively. As expected and inferred from these data, the reattachment point moves downstream as mass-injection rate increases (see Fig. 4.2).

Comparing the runs performed with injection of pure argon (higher density ratio) in Fig. 4.16 to those performed using a density-matched helium/argon mixture in Fig. 4.1, one can see that the reattachment point for pure argon injection is further upstream (the stall transition bubble is smaller). This can be explained through the growth laws for shear layers. As the density ratio is increased, the shear layer grows faster (Dimotakis 1991), hence entraining more fluid and attaching further upstream. Note that the U_{max} obtained were almost the same in both cases (Fig. 4.1 and Fig. 4.16).

CHAPTER 5

Conclusions

Experimental investigation of several aspects of mass injection in inclined subsonic diffuser was undertaken in the GALCIT Supersonic Shear Layer Facility. These consisted of both one-stream and two-stream flow non-reacting experiments, varying the mass injection velocities and the density ratio of the flow. This work focused on the study of the downstream velocity profile to explain the behavior of mass injection in a subsonic diffuser.

Individual conclusions summarizing the findings of each part of the study are found following each chapter. A summary is given below.

Top-stream flow only – For a subsonic diffuser, as the high-speed section velocity increases (zero velocity at low-speed section), the reattachment point of the separation bubble moves downstream (increased). So, the separation bubble is weakly dependent on the Reynolds number.

Two-stream flow at the same density ratio – Keeping the high-speed section at fixed speed, as the velocity in the low-speed section increases, the reattachment point of the separation bubble moves downstream. Keeping the same velocity ratio (low- and high-speed sections), as the speed increases, the reattachment point moves further downstream. As the reattachment point of the separation bubble moves downstream, the diffuser pressure coefficient decreases and therefore, the performance of the diffuser becomes worse. At a velocity ratio of around 0.321, a classical shear layer flow was observed in the facility.

Two-stream flow for higher density ratio – Comparing the density-matched experiments with a higher density ratio (keeping the same velocities for both low- and high-speed section), as the density ratio increases, the reattachment point of the

separation bubble moves upstream due to higher entrainment requirement for the shear layer. This is because as density ratio increases, the shear layer grows faster, hence entraining more fluid and attaching further upstream.

References

BOND, C. L. 1998 "Reynolds Number Effects on Mixing in the Turbulent Shear Layer," Ph.D. thesis, California Institute of Technology.

DIMOTAKIS, P. E. 1986 "Two-Dimensional Shear-Layer Entrainment," *AIAA J.* **24**, 1791-1796.

DIMOTAKIS, P. E. 1991 "Turbulence Free Shear Layer Mixing and Combustion," *High-Speed Flight Propulsion Systems,* in *Progress in Astronautics and Aeronautics, AIAA* **137**, Ch. 5, 265-340.

FOX, R. W. and KLINE, S. J. 1962 "Flow Regime Data and Design Methods for Curved Subsonic Diffusers," *J. of Basic Engineering.* **40**, 303-312.

FOX, R. W. and McDONALD, A. T. 1992 Introduction to Fluid Mechanics (4th ed., John Wiley & Sons, Inc., New York).

HALL, J. L. 1991 "An Experimental Investigation of Structure, Mixing and Combustion in Compressible Turbulent Shear Layers," Ph.D. thesis, California Institute of Technology.

HALL, J. and DIMOTAKIS, P. E. 1989 "Design Overview of the Supersonic Hydrogen-Fluorine Facility (V4.0)," GALCIT Internal Report.

LOEHRKE, R. I. and NAGIB, H. M. 1972 Experiments on Management of Free-Stream Turbulence. AGARD-R-598.

MILLER, R. W. 1985 Flow Measurement Engineering Handbook (2nd ed., McGraw-Hill, New York).

ROUSE, A. and INCE, S. 1957 "History of Hydraulics" (Iowa Institute of Hydraulics Research, State University of Iowa, Iowa City).

SINHA, S. N., GUPTA, A. K. and OBERAI, M. M. 1981 "Laminar Flow over Backsteps and Cavities, Part I: Backsteps," *AIAA J.* **19**(2), 1527-1530.

SLESSOR, M. D. 1998 "Aspects of Turbulent-Shear-Layer Dynamics and Mixing," Ph.D. thesis, California Institute of Technology.

SLESSOR, M. D. 2001 Personal communication.

SONG S., DeGRAAFF, D. B., and EATON, J. K. 2000 "Experimental Study of a Separating, Reattaching, and Redeveloping Flow over a Smoothly Contoured Ramp," *International J. Heat and Fluid Flow*, special edition, accepted.

WESTPHAL, R.V., JOHNSTON, J. P. and EATON, J. K. 1984 "Experimental Study of Flow Reattachment in a Snigle-Sided Sudden Expansion," NASA Contractor Report 3765.

WHITE, F. 1999 Fluid Mechanics (4th ed., WCB McGraw-Hill, New York).